Surfactant-Assisted Etching in Biomimetic Mineralization of Ferric Phosphate

Yu Zhao, Yi Xie,* Si Yan, and Xi Zhu

Division of Nano-materials and Nano-chemistry, Hefei National Laboratory for Physical Sciences at Microscale, University of Science and Technology of China, Hefei, Anhui 230026, P. R. China

Received January 24, 2008. Revised Manuscript Received April 4, 2008

A solution-based etching process often takes place in remodeling natural minerals and building natural wonders such as stalactites and stalagmites. Enlightened by this spontaneous mineralization process, we proposed a surfactant-assisted etching in biomimetic mineralization aiming at a better imitation of natural environments for constructing complex and extraordinary architectures of ferric phosphate. The mineralization process is achieved by thermally aging soluble ferric and phosphate salts with the existence of cetyltrimethylammonium bromide (CTAB) as surfactant. Based on the experimental evidence, the generation of such architectures relies on the competition between acidity-induced etching and selective protection by surfactant adsorption. This novel structure represents a new member with a hollow interior in the family of various micro/nanostructures and indicates that materials with attractive patterns can be readily achieved through this strategy.

Introduction

The generation of natural minerals such as coral reefs, diatomite, skeletons, etc., is attributed to biomineralization, where chemistry, biology, medicine, and materials science overlap.[1] Although significant advances have been achieved in understanding the mechanisms of biomineralization,[2] ineluctable difficulties still remain for material researchers to make natural materials following such natural ways. Therefore, a mimetic approach aiming at controllable fabrication of materials with multifarious shapes and functions has been put forward. In principle, a biomimetic mineralization approach, in which a functionalized organic additive is exposed to an aqueous solution of soluble inorganic precursors of the desired inorganic material to synthetic analogues of natural composites, offers much promise in controlling the size, shape, orientation, and crystal structure of inorganic compounds,[3] a variety of superstructured crystals can thus be readily obtained for material synthesis.[4] Generally, in situ nucleation of crystals and accumulation of basic building blocks by means of block-copolymer aggregation, surfactant micelles, microemulsions, etc., are involved in biomimetic mineralization to form highly organized crystallites.[5] Meanwhile, to design and fabricate artificial crystals, solution-based chemical etching provides an effective method for surface modification and benefits the generation of fine structures from integrated crystals.[6] The difference between solution-based chemical etching and mineralization process generally exists in the way they building crystals: etching is a top-down process which creates fine structures by decomposition of integrated crystals, whereas mineralization is a bottom-up process, which generates complex architectures through self-assembled building blocks. Though the two processes have been applied to produce the artificial crystals with exquisite and well-defined morphology,[4,6] they usually occur simultaneously in the evolvement of the natural minerals. The most well-known examples of these natural masterpieces are stalactites and stalagmites. Thus, the chemical-etching-involved biomimetic mineralization can be regarded as an effective and reasonable method to make natural materials with attractive patterns and advanced functions.

Enlightened by this spontaneous mineralization process, we tried to mimic natural environments for the formation of natural materials, ferric phosphate as an example, and a method aiming at introducing a surfactant-assisted etching process into the biomimetic mineralization was thus proposed. The driving force of etching could be provided by an enhanced acidic condition, which takes advantage of the

* To whom correspondence should be addressed. Fax: 86 551-3603-987. E-mail: yxie@ustc.edu.cn

(1) Mann, S. In *Biomineralization: Principles and Concepts in Bioinorganic Materials Chemistry*; Oxford University Press: New York, 2001.

(2) (a) Fritz, M.; Belcher, A. M.; Radmacher, M.; Walters, D. A.; Hansma, P. K.; Stucky, G. D.; Morse, D. E.; Mann, S. *Nature* **1994**, *371*, 49–51. (b) Shenton, W.; Pum, D.; Sleytr, U. B.; Mann, S. *Nature* **1997**, *389*, 585–587. (c) Banfield, J. F.; Welch, S. A.; Zhang, H. Z.; Ebert, T. T.; Penn, R. L. *Science* **2000**, *289*, 751–754. (d) Politi, Y.; Arad, T.; Klein, E.; Weiner, S.; Addadi, L. *Science* **2004**, *306*, 1161–1164.

(3) Boal, A. K.; Headley, T. J.; Tissot, R. G.; Bunker, B. C. *Adv. Funct. Mater.* **2004**, *14*, 19–24.

(4) (a) Lin, J.; Cates, E.; Bianconi, P. A. *J. Am. Chem. Soc.* **1994**, *116*, 4738–4745. (b) Li, M.; Schnablegger, H.; Mann, S. *Nature* **1999**, *402*, 393–395. (c) Cha, J. N.; Stucky, G. D.; Morse, D. E.; Deming, T. J. *Nature* **2000**, *403*, 289–292. (d) Cölfen, H.; Mann, S. *Angew. Chem., Int. Ed.* **2003**, *42*, 2350–2365. (e) Shi, H. T.; Qi, L. M.; Ma, J. M.; Cheng, H. M. *J. Am. Chem. Soc.* **2003**, *125*, 3450–3451. (f) Yu, S. H.; Cölfen, H.; Tauer, K.; Antonietti, M. *Nat. Mater.* **2005**, *4*, 51–55. (g) Wang, T. X.; Xu, A. W.; Cölfen, H. *Angew. Chem., Int. Ed.* **2006**, *45*, 4451–4455.

(5) Xu, A. W.; Ma, Y. R.; Cölfen, H. *J. Mater. Chem.* **2007**, *17*, 415–449.

(6) (a) Li, F.; Ding, Y.; Gao, P.; Xin, X.; Wang, Z. L. *Angew. Chem., Int. Ed.* **2004**, *43*, 5238–5242. (b) Jia, C. J.; Sun, L. D.; Yan, Z. G.; You, L. P.; Luo, F.; Han, X. D.; Pang, Y. C.; Zhang, Z.; Yan, C.-H. *Angew. Chem., Int. Ed.* **2005**, *44*, 4328–4333. (c) Im, S. H.; Lee, Y. T.; Wiley, B.; Xia, Y. N. *Angew. Chem., Int. Ed.* **2005**, *44*, 2154–2157. (d) Chen, J. Y.; McLellan, J. M.; Siekkinen, A.; Xiong, Y. J.; Li, Z. Y.; Xia, Y. N. *J. Am. Chem. Soc.* **2006**, *128*, 14776–14777.

10.1021/cm8002468 CCC: $40.75
Published on Web 05/30/2008

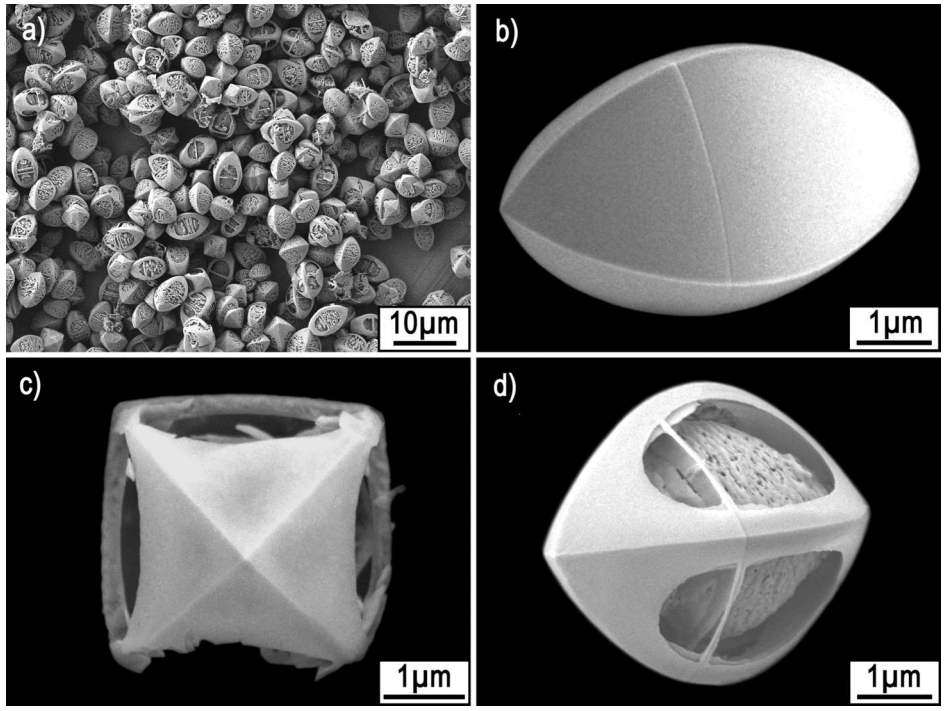

Figure 1. Electron microscopy images of the product obtained at 220 °C for 12 h with CTAB concentration of 15 mmol L^{-1} and pH of 1.5: (a) low-magnification SEM image revealing the high yield and uniform size distribution of the rugby-like product; (b−d) high-magnification SEM images showing the spindlelike surface, the sharp vertex and arrises, and the elliptical hole centered in the unit plane, respectively.

proton release from hydrophosphate ions during the mineralization process. By thermally aging a CTAB solution containing soluble ferric and phosphate precursors under proper acidity, extraordinary architectures of ferric phosphate could be readily obtained simply via this surfactant-assisted etching process in biomimetic mineralization.

Materials and Methods

Sample Synthesis. All chemicals were of analytical grade and used without further purification. In a typical procedure, cetyltrimethylammonium bromide (CTAB, 0.273 g, 0.75 mmol) was dissolved into 40 mL of distilled water with constant stirring for 30 min to give a homogeneous solution. Then ammonium iron(III) sulfate ($NH_4Fe(SO_4)_2 \cdot 12H_2O$, 0.482 g, 1.0 mmol) and trisodium phosphate ($Na_3PO_4 \cdot 12H_2O$, 0.380 g, 1.0 mmol) were added into the 40 mL of homogeneous solution. The pH value of the cloudy solution was adjusted to ca. 1.5 by carefully adding sulfuric acid (H_2SO_4, 5 M). The total volume of the precursor solution was adjusted to 50 mL with distilled water and stirred for another 30 min before being transferred into the pretreated Teflonlined stainless-steel autoclave. The autoclave was heated to 220 °C at the heating rate of 5 °C min^{-1} and maintained at 220 °C for 12 h. After cooling, the as-prepared light-green precipitate was collected and washed with distilled water and acetone several times and dried in a vacuum at 60 °C for 6 h.

Sample Characterization. The sample was characterized using XRD with Philips X'Pert Pro Super diffractometer with Cu Kα radiation (λ = 1.54178 Å). TGA analysis was carried out on a Shimadzu TA-50 thermal analyzer at a heating rate of 10 °C min^{-1}. XPS measurements were performed on a VGESCALAB MKII X-ray photoelectron spectrometer with an excitation source of Mg Kα = 1253.6 eV. The field emission scanning electron microscopy (FE-SEM) images were taken on a JEOL JSM-6700F scanning electron microscope. The transmission electron microscopy (TEM) images were obtained on Hitachi H-800 transmission electron microscope at an acceleration voltage of 200 kV. High-resolution transmission electron microscopy (HRTEM) images, SAED patterns and energy-dispersive X-ray spectroscopy (EDX) analysis were performed on JEOL-2010 transmission electron microscope at an acceleration voltage of 200 kV. The FTIR experiments were carried out on a Bruker Vector-22 FTIR spectrometer (Bruker Instruments, Billerica, MA) in a KBr pellet, scanning from 4000 to 400 cm^{-1} at room temperature.

Results and Discussion

Figure 1a presents a panoramic scanning electron microscopy (SEM) image of the as-obtained product showing a high yield and uniform size distribution. The particles turn out to have a peculiar rugby-like morphology with length of 6−8 μm and radius of 3−4 μm. Magnified SEM images showing the surface, shell vertex and elliptical holes in the shell are severally presented in Figure 1b−d. The shell shown in Figure 1b possesses a very smooth surface and is constructed from four spindle-like unit planes, which show an impressive range of curvature. The unit planes precisely converge at the both ends of the rugby and thus form the obvious vertices as well as the arrises as shown in Figure 1c. In most cases, the unit plane has an elliptical hole spreading out around its center as shown in Figure 1d, through which the internal structure can be clearly observed. Interestingly, the rugby usually has "waist belt" athwart at the elliptical holes, and both ends of the waist belt blend naturally into the spindlelike planes as observed in both images a and d in Figure 1. Corresponding XRD analysis (see the Supporting Information, Figure S1-1) indicates that the as-obtained product is phase-pure iron phosphate hydroxide with a monoclinic lattice (space group *C*2/*c*). X-ray photoelectron spectroscopy

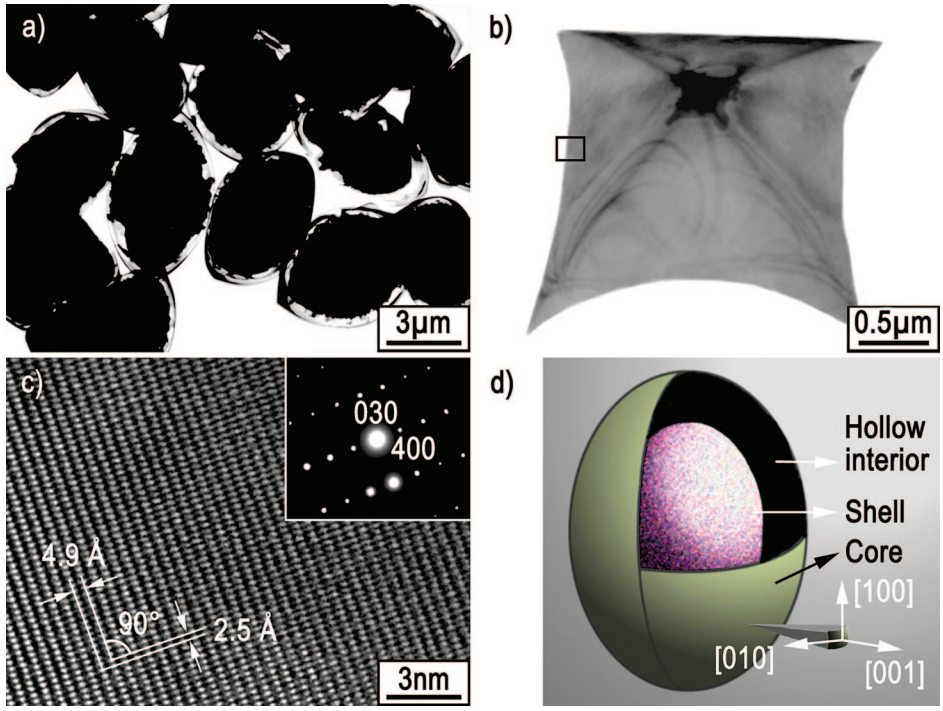

Figure 2. TEM images of (a) the rugby and (b) a desquamated shell vertex. (c) HRTEM image and corresponding SAED pattern (inset) recorded in the framed area in part (b). The lattice spacing of 4.9 and 2.5 Å between adjacent lattice planes corresponds to the distance of adjacent {400} and {030} crystal planes. (d) Simulated model of the rugby summarizing the structural information.

(XPS) (see the Supporting Information, Figure S1-2) reveals the average atomic ratio of Fe, P, and O in the product is about 1.37:1:5.2 on the basis of the quantification of Fe_{2p}, P_{2p}, and O_{1s} peaks, consistent with the stoichiometric proportion of iron phosphate hydroxide. A weak signal of N_{1s} is observed in the survey XPS spectrum, which can be assigned to the surface absorption of CTAB molecules. Thermogravimetric analysis (TGA) (see the Supporting Information, Figure S1-3) reveals a favorable thermostability of the product to as high as ca. 300 °C and shows a total weight loss of 4.6% compared with the theoretical value of ca. 4.8%, which arises from a complete decomposition to $FePO_4$, Fe_3PO_7, and H_2O elimination.[7]

The semihollowed character of the rugby and crystallinity of the shell are confirmed by transmission electron microscopy (TEM) and high-resolution TEM (HRTEM) as shown in Figure 2a−c. Figure 2a shows a typical TEM image of the rugby, where the hollow interior between the shell and core can be clearly observed. The TEM image of a desquamated shell vertex is presented in Figure 2b. The arrises are obvious and converge at the shell vertex, which consists with the SEM observation. The crystallinity and orientation of a unit plane are further investigated by HRTEM as shown in Figure 2c. The clear lattice image and the sharp diffraction spots (inset) indicate the high crystallinity of the plane. The unit plane is single crystalline and shows preferential growth directions of [100] along its long axis and [010] along its minor axis. All four unit planes have the same structure, whereas the entire shell turns out to be not a single crystal (see the Supporting Information, Figure S2). In the HRTEM study, dislocation or boundary[8] has not been observed in the region where the unit plane intersects (vertex and arrises). We suggest that the structure of the shell can be considered as surrounding by four {001} oriented single-crystallined unit planes with faceted surface between each adjacent unit planes. Corresponding EDX analysis on the desquamated shell confirms that only Fe, P, and O elements exist, with a P:Fe atomic ratio of c.a. 1:1.39 (see the Supporting Information, Figure S3). Figure 2d presents a simulated model summarizing the structural information of the rugby.

In our study, the final morphology of the product strongly depends on some kinetic parameters such as pH value, temperature, and CTAB concentration. Meanwhile, the foreign ions such as NH_4^+, Na^+, and SO_4^{2-} introduced by the soluble ferric and phosphate salts hardly affect the formation of the rugby (see the Supporting Information, Figures S4-1 and S4-2). Further investigation into the formation process of the rugby is conducted by examining their earlier growth stages. The corresponding TEM images and XRD patterns are displayed in Figure 3a−e and the Supporting Information, Figure S1-1, respectively. The morphology evolution undergoes a gradual etching process with prolonged reaction time. The etching starts from the surface, penetrates into the interior, and excavates around the center. Semihollowed rugby can be obtained when the reaction time is in excess of 12 h. The shape evolution is schematically illustrated in Figure 3f.

The growth of semihollowed rugby involves a fast mineralization and a slow etching process. In the former process, polyhedral particles have formed and the acidity of the system decreases due to the hydrophosphate ions exhaustion. The enhanced acidity plays a crucial role in the

(7) Torardi, C. C.; Reiff, W. M.; Takacs, L. *J. Solid State Chem.* **1989**, *82*, 203–215.

(8) (a) Wiley, B.; Sun, Y.; Mayers, B.; Xia, Y. *Chem.—Eur. J.* **2005**, *11*, 454–463. (b) Sánchez-Iglesias, A.; Pastoriza-Santos, I.; Pérez-Juste, J.; Rodríguez-González, B.; Javier García de Abajo, F.; Liz-Marzán, L. M. *Adv. Mater.* **2006**, *18*, 2529–2534.

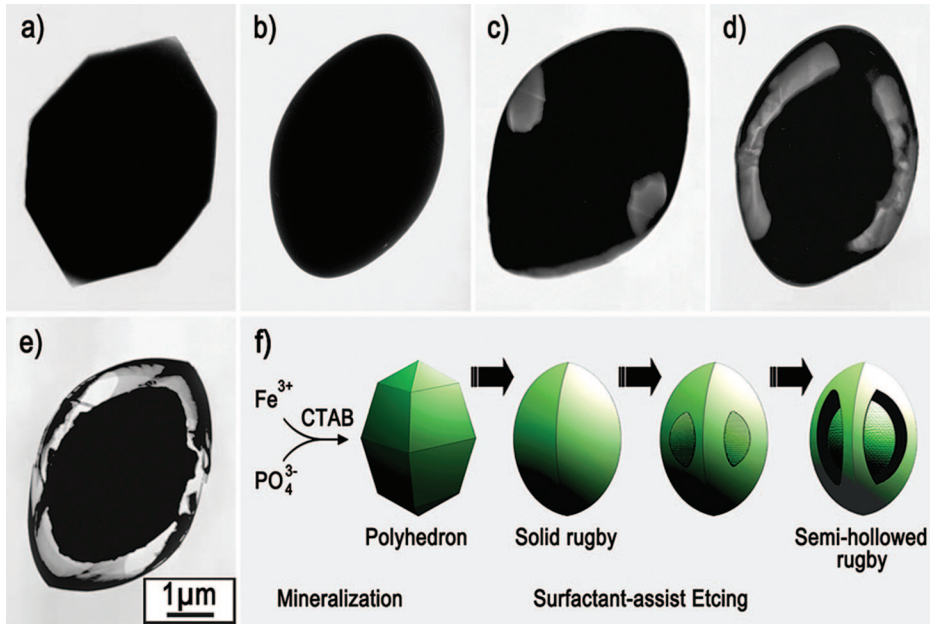

Figure 3. (a−e) TEM images showing the shape evolution of intermediates with prolonged reaction time for 45 min and 1, 2.5, 6, and 12 h, respectively. The corresponding XRD patterns are presented in the Supporting Information, Figure S1-1. (f) Schematic illustration of the rugby formation process.

morphology evolution of these particles to transform into rugby-like particles, because no rugby-like particle has been observed when the pH value is increased as shown in the Supporting Information, Figure S4-1a−c. The self-enhanced acidity enables the polyhedrons to be etched by means of rounding off their vertices and arrises to form the solid rugby with coherence interface to minimize the interface energy.[9] Meanwhile, the adsorption of CTAB also plays an important role in remodeling the shape of the polyhedrons, compared with which the size, vertices, and arrises are perfectly inherited from the solid rugby (see the Supporting Information, Figure S5 and section S5). The following shape transformation from solid to semihollowed rugby strongly depends on the competition between etching and capping. The etching tends to decompose the particles, whereas the adsorbed CTAB molecules stabilize the particle surface and prevent the surface from being etched. Once a pit has formed on the surface, further corrosion would occur preferentially inside the pit. As etching continues, the concentration of hydrophosphate ions is sufficiently increased. In other words, the concentration of protons is decreased and thus leads to the weakening of etching. As the etching and capping proceeds, semihollowed rugby has formed. It is worth pointing out that chemical-etching-involved mineralization accompanying the adsorption phenomenon has also been observed in the synthesis of α-Fe_2O_3 nanotubes[6b] and octahedral Cu_2O nanocages.[17] However, in our approach, the driving force of etching arises from the enhancement of acidity.

To understand where the etching should start and where the CTAB molecules should absorb in the formation process of the semihollowed rugby, we start from the crystal structure of $Fe_4(PO_4)_3(OH)_3$. Figure 4a shows a schematic crystal structure of $Fe_4(PO_4)_3(OH)_3$ super cell ($2 \times 6 \times 1$ slabs) projected along the *c* axis, in which there are aligned tunnels distributing regularly along the [010] direction. The negatively charged PO_4 tetrahedron and FeO_6 octahedron is neutralized by H^+ in the innerspace of the tunnel and thus facilitate the etching to take place in these tunnels. As a macroscopically reflection, the surfaces of the particles that have been etched for 4 h as shown in Figure 4b are filled with parallel nicks aligned along the same direction. According to the HRTEM and crystal structure analysis, this direction is consistent with the [010] direction of the single-crystalline unit plane and the direction of the aligned tunnels. The formation of the nicks can be regarded as etching and decomposition of PO_4 tetrahedrons and FeO_6 octahedrons along the aligned tunnels. Similar phenomenon has also been observed in the syntheses of $H_2Ti_3O_7$[10] nanotubes and hyperbranched $BiVO_4$,[11] where the crystal has lamellar structure or aligned tunnels. As to the adsorption of CTAB on the formation of the shell, there must to be a strong interaction between CTAB $C-N^+$ headgroups and the surface oxygen anions, because the shell remains stable compared with the shrunk core shown in Figure 4c even if the reaction time has been prolonged to 24 h. Relevant HRXPS analysis shown in Figure 5 confirms such a strong interaction between the surface oxygen anions and $C-N^+$ headgroups of CTAB molecule. There are three carbon contributions existed in the C_{1s} region of CTAB (Figure 5a): the core levels centered at 284.6, 285.7, and 286.6 eV can be severally assigned to calibrated hydrocarbon, the carbon in the methylene chain (C_2-C_{16}) and headgroup-carbon ($(CH_3)_3-N^+-CH_2-$).[12] In the C_{1s} region of the product

(9) (a) Wang, Z. L.; Feng, X. *J. Phys. Chem. B* **2003**, *107*, 13563–13566. (b) Kwon, S. G.; Piao, Y.; Park, J.; Angappane, S.; Jo, Y.; Hwang, N. M.; Park, J. G.; Hyeon, T. *J. Am. Chem. Soc.* **2007**, *129*, 12571–12584.

(10) Zhang, S.; Peng, L. M.; Chen, Q.; Du, G. H.; Dawson, G.; Zhou, W. Z. *Phys. Rev. Lett.* **2003**, *91*, 256103.

(11) Zhao, Y.; Xie, Y.; Zhu, X.; Yan, S.; Wang, S. *Chem.—Eur. J.* **2008**, *14*, 1601–1606.

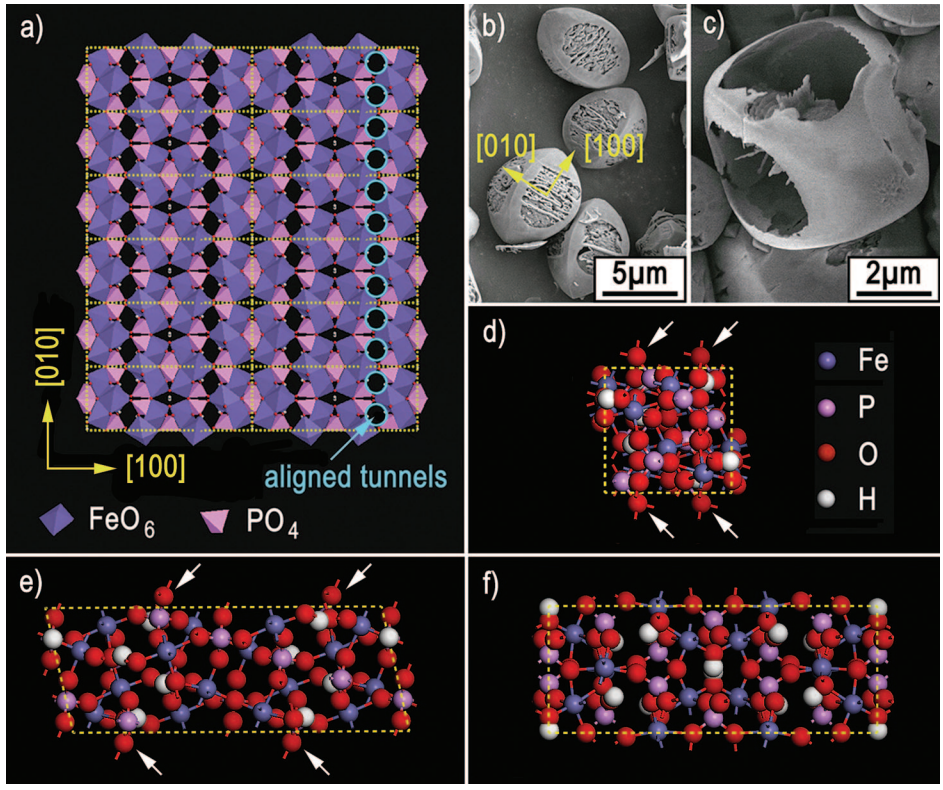

Figure 4. (a) Schematic crystal structure of $Fe_4(PO_4)_3(OH)_3$ super cell ($2 \times 6 \times 1$ slabs) projected along the *c* axis. (b) and (c) SEM image of the samples collected after the precursor solution has been thermally aged for 4 and 24 h, respectively. (d−f) Schematic crystal structure of $Fe_4(PO_4)_3(OH)_3$ unit cell projected along the *a*, *b*, and *c* axis, respectively. The crystal structure is simulated according to the crystallographic data in ref 7 and the values given by the Inorganic Crystal Structure Database (ICSD 72726).

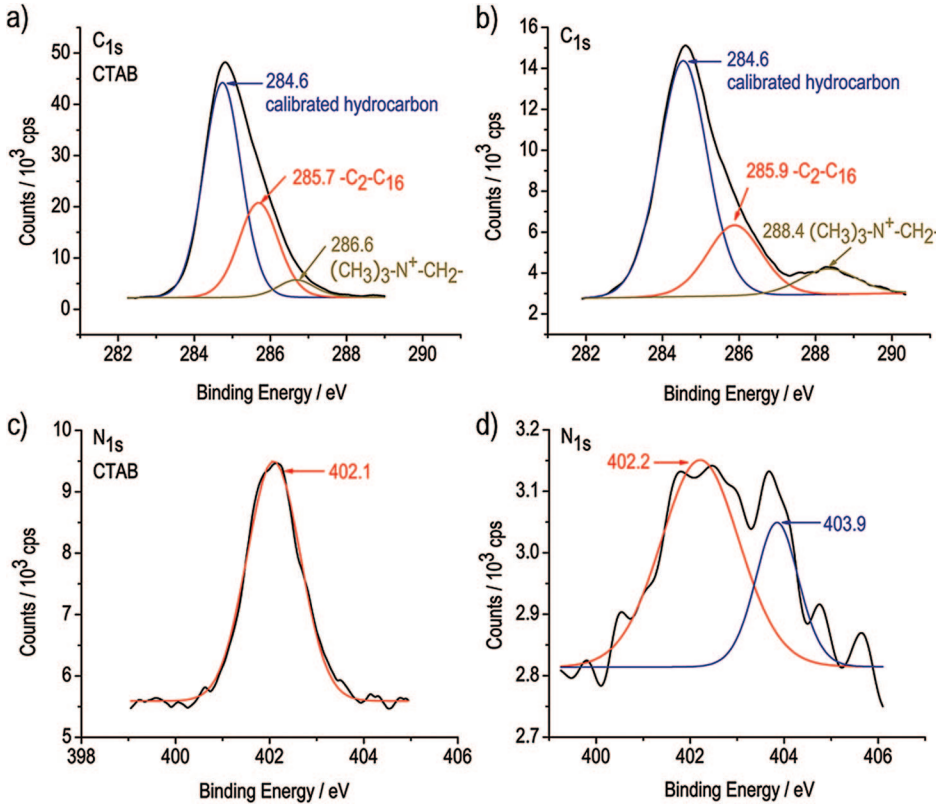

Figure 5. HRXPS spectra of C_{1s} and N_{1s} region. (a, b) Characteristic C_{1s} core line signals of CTAB and as-synthesized product, respectively; (c, d) characteristic N_{1s} core line signals of CTAB and the as-synthesized product, respectively.

(Figure 5b), the core level of carbon in the methylene chain seems hardly changed (285.9 eV in CTAB and 285.7 eV in the product). However, the core level of the headgroup-carbon shows a movement (1.8 eV) to higher binding energy levels, indicating a strong interaction between the CTAB headgroup and oxygen anions in the rugby's surface. The

N_{1s} core level of CTAB centers at 402.1 eV (Figure 5c), whereas there are two nitrogen contributions existed in the N_{1s} region of the product centering at 402.2 and 403.9 eV, respectively (Figure 5d). The binding energy of 403.9 eV can be assigned to the $C-N^+$ headgroup that interacts with oxygen anions in rugby's surface resulting in the movement to higher binding energy levels, because the counterion of the $C-N^+$ headgroup is changed from Br^- to oxygen anions, which possess higher electronegativity than Br^-, and thus the binding energy of N_{1s} has been increased. The binding energy of 402.2 eV can be appointed to the headgroups toward the water environment in the double layer arrangement as documented elsewhere.[12c,13] Such an interaction can also be confirmed by FTIR analysis (see the Supporting Information, Figure S6).

Although the exact bonding geometry for surfactant molecules is still not clear,[14] some clues leading to further understanding the nature of adsorption selectivity of CTAB can be provided by the analysis of oxygen anion distribution in different crystallographic planes. Figure 4d−f present the schematic crystal structure of $Fe_4(PO_4)_3(OH)_3$ unit cell projected along the *a*, *b*, and *c* axis, respectively. The oxygen anions (signed with an arrow) located in (001) planes possess weaker steric effect and can interact easier with CTAB $C-N^+$ headgroup compared with the others. We deduce such an oxygen−anion configuration facilitates the adsorption of CTAB on (001) planes. Therefore, the adsorption capacities and affinities for CTAB to the surface are higher for the (001) planes than for the others, and the adsorbed CTAB will protect them from further reaction. In comparison, we have tried to use noncationic surfactants including poly(vinylpyrrolidone) (PVP), dodecyl benzene sulfonic acid sodium salt (DBS), polyacrylamide (PAA), and polyethylene glycol 1000 to mimic the mineralization of ferric phosphate. All of them have little effect that really benefits the formation of rugby-like morphology (see the Supporting Information, Figure S7). However, when tetradecylpyridinium bromide (TPB), which possesses a similar $C-N^+$ headgroup with CTAB, is introduced to instead of CTAB, rugby-like product can be readily obtained (see the Supporting Information, Figure S8). Hence, the co-operation of etching and capping in {001} terminated surface of the rugby is responsible for the formation of such a peculiar structure. Unlike the prevalent patterns formed by surfactant-assisted controllable growth[15] or other classic patterns with impressive surface curvature,[16] the generation of rugby-like morphology in our case has a distinctive style, which is attributable to the introduction of an etching process into the realm of biomimetic mineralization.

In conclusion, to better mimic the natural environments for the formation of natural materials, we have proposed a surfactant-assisted etching in biomimetic mineralization of ferric phosphate with peculiar structure. This structure differs from the reported ones and represents a new kind of material with hollow interior in the family of various micro/nanostructures. The introducing of a chemical etching process into biomimetic mineralization greatly benefits the generation of attractive and extraordinary architectures.

Acknowledgment. This work was financially supported by the National Natural Science Foundation of China (20621061). The authors thank Mr. Linfeng Fei and Dr. Shudong Zhang for help with TEM and SEM studies, respectively.

Supporting Information Available: XRD, XPS, TGA, EDX, and FTIR analysis; SEM, TEM, HRTEM images; and crystal structure (PDF). This material is available free of charge via the Internet at http://pubs.acs.org.

CM8002468

(12) (a) Beamson, G.; Briggs, D. In *High Resolution XPS of Organic Polymers, the Scienta ESCA 300 Database*; John Wiley & Sons: New York, 1992. (b) Lindberg, B. J.; Hedman, J. *J. Chem. Scr.* **1975**, *7*, 155–166. (c) Nikoobakht, B.; El-Sayed, M. A. *Langmuir* **2001**, *17*, 6368–6374.
(13) Richetti, P.; Kékicheff, P. *Phys. Rev. Lett.* **1992**, *68*, 1951–1954.
(14) Sun, Y.; Xia, Y. *Science* **2002**, *298*, 2176–2179.
(15) (a) Kuang, D.; Xu, A.; Fang, Y.; Liu, H.; Frommen, C.; Fenske, D. *Adv. Mater.* **2003**, *15*, 1747–1750. (b) Nikoobakht, B.; El-Sayed, M. A. *Chem. Mater.* **2003**, *15*, 1957–1962. (c) Xu, H. L.; Wang, W. Z. *Angew. Chem., Int. Ed.* **2007**, *46*, 1489–1492. (d) Xu, Z.; Hou, Y.; Sun, S. *J. Am. Chem. Soc.* **2007**, *129*, 8698–8699. (e) Yang, S.; Zhou, X.; Yuan, P.; Yu, M.; Xie, S.; Zou, J.; Lu, G. Q.; Yu, C. *Angew. Chem., Int. Ed.* **2007**, *46*, 8579–8582.
(16) (a) Yang, H.; Coombs, N.; Ozin, G. A. *Nature* **1997**, *386*, 692–695. (b) Sano, M.; Kamino, A.; Okamura, J.; Shinkai, S. *Science* **2001**, *293*, 1299–1301. (c) Kong, X. Y.; Ding, Y.; Yang, Y.; Wang, Z. L. *Science* **2004**, *303*, 1348–1351. (d) Gao, P. X.; Ding, Y.; Mai, W.; Hughes, W. L.; Lao, C.; Wang, Z. L. *Science* **2005**, *309*, 1700–1704.
(17) Lu, C.; Qi, L.; Yang, J.; Wang, X.; Zhang, D.; Xie, J.; Ma, J. *Adv. Mater.* **2005**, *17*, 2562–2567.